

# A Detailed Study on Light-Induced Degradation of Cz-Si PERC-Type Solar Cells: Evidence of Rear Surface-Related Degradation

Axel Herguth , Christian Derricks , and David Sperber 

**Abstract**—A light-induced degradation phenomenon of unknown origin in p-type Cz-Si passivated emitter and rear cell (PERC)-type solar cells is thoroughly investigated by collating results from different measurement techniques and predictions from various simulations. The observed degradation manifests in slight losses in  $j_{sc}$ , strong losses in  $V_{oc}$ , and devastating losses in FF, and thus massively impacts efficiency. It is found that the series resistance degrades significantly due to a degradation of front contact resistance. This, however, does not explain losses in  $V_{oc}$  and  $j_{sc}$ , which are attributed to the degradation of a different cell component. Neither a degradation by defect formation in the space charge region, nor the emitter, nor the bulk is found to consistently explain the observations. Only a rear surface-related degradation mechanism explains consistently all experimental findings.

**Index Terms**—Light-induced degradation (LID), passivated emitter and rear cell (PERC) silicon solar cells, simulation, surface-related degradation (SRD).

## I. INTRODUCTION

IN RECENT years, the efficiency of silicon wafer-based solar cells has been steadily improved by process optimization and design adaptations, e.g., [1] and [2]. Especially, the development of the passivated emitter and rear cell (PERC) concept [3] up to market maturity has boosted reported efficiencies in industrial pilot lines and mass production to remarkable (non-degraded) 21% and beyond for monocrystalline silicon grown by Czochralski's method (Cz-Si), e.g., [1]. The advantage of PERC-type solar cells over “conventional” full-area rear-side Al-alloyed solar cells originates from an improved passivation quality at the dielectrically passivated rear surface interrupted only locally by Al-alloyed contacts allowing PERC-type solar cells to benefit from higher bulk minority charge carrier lifetimes otherwise capped by a poor rear-side passivation.

Unfortunately, this higher sensitivity is also their downside: PERC-type cells are more vulnerable to either poor material quality and/or poor passivation quality. In addition, the higher

solar cell efficiency (potential) comes at the price of higher process complexity and hence higher production costs. Therefore, PERC-type solar cells require—from an economic point of view—good material quality and rear surface passivation as they not only need to match the efficiency of conventional solar cells but have to outperform them to a certain degree.

In contrast to poor quality wafers that may be identified and rejected by incoming control, light-induced degradation (LID) phenomena, occurring at first in the finished solar cell even made of apparently high-quality material, pose a serious problem worsening the better the solar cell gets if no countermeasures are applied. In the literature, a long list of different types of LID can be found, e.g., boron-oxygen-related (BO-) LID mainly affecting oxygen-rich Cz-Si [4]–[14], FeB pairing and dissociation mainly affecting mc-Si and sometimes Cz-Si as well [16]–[18], Cu-LID mainly affecting mc-Si [15], sponge LID found only in mc-Si [19], light and elevated temperature induced degradation (LeTID) mainly affecting mc-Si [20]–[25] and probably Cz-Si as well [1], [26], and LID in FZ-Si [27]–[29] (being probably LeTID as well [30], [31]) to mention the most frequently encountered. Besides that, surface-related LID phenomena can be found as well [27], [32]. In light of the multitude of already reported LID phenomena, it is sometimes challenging to identify the effect at work.

Within this contribution, LID of unknown origin in p-type Cz-Si PERC-type solar cells is thoroughly investigated by collating results from different measurement techniques and predictions from various simulations. Although some conclusions can be drawn qualitatively from the measurements even without detailed simulations, we find it instructive to explain and quantify these conclusions on the basis of detailed simulations.

## II. FIRST EXPERIMENTAL FINDINGS

In an earlier study [33], it was found that the open-circuit voltage  $V_{oc}$  of boron-doped ( $1.3 \Omega \cdot \text{cm}$ ) Cz-Si wafer-based ( $\sim 145 \mu\text{m}$ ) PERC-type industrially made solar cell with  $\text{SiO}_x/\text{SiN}_x\text{:H}$  rear-side passivation and screen-printed metalization (3 busbar, H-pattern, fired in a belt furnace) showed noticeable degradation (and subsequent recovery) when subjected to illumination (halogen incandescent lamps,  $\sim 1$  sun current equivalent [34], open-circuit conditions) at elevated temperature ( $150^\circ\text{C}$ ), as reproduced in Fig. 1. While the first drop and recovery is attributed to the formation and

Manuscript received March 8, 2018; revised April 30, 2018 and June 16, 2018; accepted June 19, 2018. This work was supported by the German Federal Ministry for Economic Affairs and Energy under Grants 0325877C, 0325763B, and 0324001. (Corresponding author: Axel Herguth.)

The authors are with the Department of Physics, University of Konstanz, Konstanz 78457, Germany (e-mail: Axel.Herguth@uni-konstanz.de; Christian.Derricks@uni-konstanz.de; David.Sperber@uni-konstanz.de).

Color versions of one or more of the figures in this paper are available online at <http://ieeexplore.ieee.org>.

Digital Object Identifier 10.1109/JPHOTOV.2018.2850521

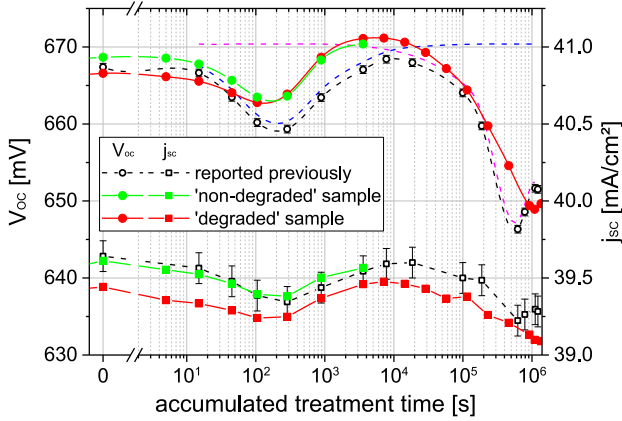


Fig. 1. Temporal evolution of  $V_{oc}$  and  $j_{sc}$  (according to STC [35]) during treatment at the elevated temperature of 150 °C, illumination of 1 sun, and open-circuit condition. Shown are  $V_{oc}$  and  $j_{sc}$  data from a previously reported study [33] together with data from additional samples used for root cause analysis. For the nondegraded and the degraded sample,  $\pm 2\sigma$  repeatability uncertainty corresponds to the symbol size. The total uncertainty of  $j_{sc}$  is  $\pm 2\%$  mainly introduced by the used calibrated reference cell.

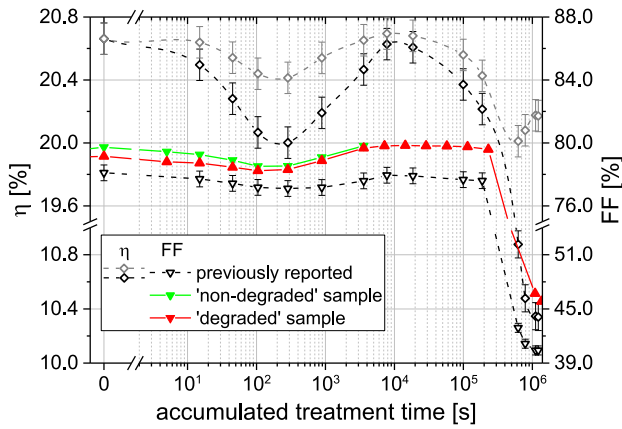


Fig. 2. Temporal evolution of  $\eta$  and FF (according to STC [35]) during treatment at the elevated temperature of 150 °C, illumination of 1 sun, and open-circuit condition. Shown are unpublished complementary data to the previously reported study [33] together with data from additional samples used for root cause analysis. Gray diamonds show  $\eta$  calculated with a fixed FF, while black diamonds show the measured  $\eta$  with varying FF. For the nondegraded and degraded sample,  $\pm 2\sigma$  repeatability uncertainty corresponds to the symbol size.

neutralization of BO-related defects [8]–[10] and maybe LeTID-related defects [26] (indicated by the blue dashed line in Fig. 1) and shall not be discussed here in detail, the root cause for the second even more severe drop and subsequent recovery in  $V_{oc}$  (indicated by the pink dashed line in Fig. 1) is unclear and subject of this contribution. For the solar cell efficiency  $\eta$ , a loss in open-circuit voltage  $V_{oc}$  and short-circuit current density  $j_{sc}$  is of course detrimental; however,  $\eta$  shown in Fig. 2 is found to suffer by far more than expectable from the loss in  $V_{oc}$  and  $j_{sc}$  alone (black versus gray dashed line in Fig. 2). The fill factor (FF) is found to drop hard during the second drop in  $V_{oc}$ , causing the main part of the efficiency loss.

One can speculate on the root cause of the observed phenomenon; however, any explanation will not only have to deal with the loss in  $V_{oc}$  and  $j_{sc}$  but also has to take the FF loss into account. Two additional equivalent cells were used for root

cause analysis. A “nondegraded” sample (green data, Fig. 1) was treated at 150 °C and 1 sun illumination (current equivalent [34], open-circuit conditions) until BO-LID (and maybe LeTID) was assumed to have recovered almost completely, but the second drop has barely started. A second “degraded” sample (red data, Fig. 1) was treated alike until the second drop has reached almost its maximal amplitude. Additional characterization was carried out with these samples, which will be discussed later on.

In the following, the term “Hi”- $V_{oc}$  is identified with  $V_{oc}$  of  $\sim 670$  mV of the degraded sample prior to the second degradation ( $\sim 7 \cdot 10^3$  s) and the term “Lo”- $V_{oc}$  for  $V_{oc}$  of  $\sim 649$  mV reached in the second minimum ( $\sim 1 \cdot 10^6$  s).

### III. ROOT CAUSE ANALYSIS

#### A. Degradation of Series Resistance?

One quite simple explanation for the loss in FF is a significant increase in series resistance  $R_s$ . One way of analyzing series resistance losses is the measurement of  $j_{sc}$ - $V_{oc}$  or Suns- $V_{oc}$  curves, where varying intensity is used to imply a varying voltage [39], [40], however without current leaving the cell. Thus, this curve is virtually free of series resistance effects and can be used to determine the series resistance free pseudo fill factor (pFF). If only  $R_s$  changes, FF will change as well, but pFF will remain unchanged.

And indeed this behavior is observed. Although the FF of the “degraded” cell drops severely from 79% to 46% (red data in Fig. 2), hence almost dragging the efficiency along into the one-digit percent range, pFF remains in the 81% range (data not shown, Suns- $V_{oc}$  tester from Sinton Instruments). This suggests that series resistance is massively impacted.

In order to track down the increase in series resistance, the different contributing factors were further analyzed for the non-degraded and the degraded sample. In principle, series resistance is a blend of line resistance along the fingers of the front-side metallization, the contact resistance of the fingers to the emitter, the emitter (sheet) resistance, the base resistance, and the contact resistance of the local rear-side contacts.

The line resistance of the fingers (screen-printed Ag paste) showed hardly any change comparing the nondegraded and the degraded sample even though the finger grid showed signs of tarnish probably due to oxidization in ambient air. Thus, a deterioration of the bulk finger can be excluded as a dominant degradation factor.

The assessment of the local Al-alloyed rear contacts via the transfer length (or transmission line) method [41], [42] showed neither a change in rear contact resistance to the base nor in base resistance between nondegraded and degraded sample. Thus, a significant contribution of the rear-side contacts to the observed increase in series resistance can be excluded as well.

The evaluation of the front-side contacts via the transfer length method revealed a significant change in contact resistance of the fingers to the emitter while the emitter sheet resistance remained unchanged. Contact resistance in the degraded sample was found to be at least a factor of 20–30 higher than in the nondegraded sample and to feature a lateral inhomogeneous distribution almost rendering the transfer length method

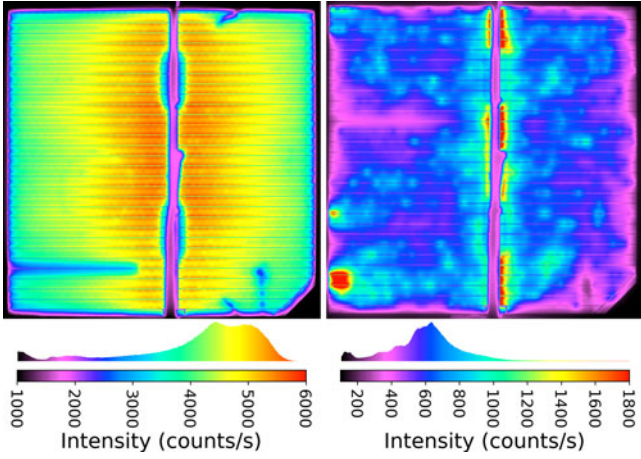


Fig. 3. Electroluminescence images including intensity histograms of a non-degraded (left) and a degraded (right) 5 cm × 5 cm subsample taken at ~670 mV excitation at 25 °C. Samples feature an unpassivated edge cut by a dicing saw. Current injection is done via multiple spring loaded pins on the continuous front busbar. The Al-covered rear side (featuring two soldering pads underneath the front busbar) was contacted on the whole area.

invalid as it relies on a similar contact resistance on a multitude of adjacent fingers.

Fig. 3 shows electroluminescence images of a nondegraded (left, corresponding to the last green data point in Figs. 1 and 2) and a degraded (right, corresponding to the last red data point in Figs. 1 and 2) subsample. In general, luminescence intensity  $\phi$  scales with the local excess charge carrier concentration  $\Delta n$  or local voltage  $V$  according to [43], [44]

$$\phi \propto n \cdot p \approx \Delta n \cdot (N_{\text{dop}} + \Delta n) \approx n_i^2 \cdot \exp\left(\frac{qV}{kT}\right) \quad (1)$$

with  $n$  and  $p$  being the total electron and hole concentration,  $N_{\text{dop}}$  being the doping concentration, and  $n_i$  being the intrinsic equilibrium carrier concentration. Furthermore,  $q$  represents the elementary charge,  $k$  Boltzmann's constant, and  $T$  the absolute temperature. As current flow across a resistance results in a voltage drop, local voltage (and thus luminescence intensity) falls below the voltage at the injection site (busbar), the stronger the higher the resistance and the higher the current flow between that point and the injection site. Fig. 3 (left) depicts for the nondegraded sample a comparably normal situation with voltage decreasing approximately quadratically with distance both along the finger and in between the fingers. For the degraded sample (Fig. 3 right), the situation has dramatically changed. Luminescence intensity originates almost only from a halo around the busbar (disrupted from two rear-side soldering pads) and a very small finger section in the lower left corner. Hardly any other finger exhibits a sufficiently good contact anymore, even though the image reveals a kind of random cloudy distribution of individual contact sites with varying quality. Especially, the few sites of good contact give the series resistance a laterally distributed nature distorting the  $j(V)$  characteristic more than a nonlaterally distributed series resistance would already do.

However, one could argue that the electroluminescence images depict not only the local voltage distribution due to a laterally distributed series resistance but also the local

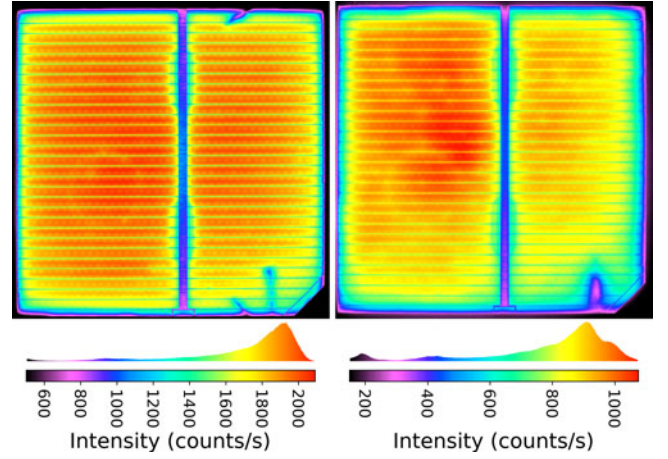


Fig. 4. Open-circuit photoluminescence images including intensity histograms taken at ~1 sun (photon flux equivalent [34], 808 nm laser illumination, 25 °C) of the same nondegraded (left) and a degraded (right) 5 cm × 5 cm subsample, as in Fig. 3. Samples feature an unpassivated edge cut by a dicing saw. The rear-side metallization exhibits two poorly passivated soldering pads underneath the front busbar.

material quality [eff. bulk lifetime,  $j_{01}$  in (2)]. The local material quality can be assessed from photoluminescence imaging under open-circuit conditions. Then, series resistance should play no role as no current is leaving the cell. However, lateral material quality variations may lead to local voltage variations, which will result in compensation currents across the series resistance. Fortunately, a high series resistance is helpful as it suppresses those compensation currents and thus helps revealing better local variations in material quality. Fig. 4 depicts open-circuit photoluminescence images taken at ~1 sun intensity (photon flux equivalent [34], 808 nm laser illumination intensity, 25 °C) of both the same nondegraded (left) and the degraded (right) subcell as used in Fig. 3. As can be seen, luminescence intensity is quite homogeneous. Equation (1) allows to deduce a voltage spread from the histograms. Besides the signal drop at the unpassivated edges (cut by a dicing saw), the luminescence intensity lies for the nondegraded sample in the range of  $1900 \pm 100$  cts/s corresponding to a voltage spread of  $\pm 1.5$  mV and for the degraded sample in the range of  $900 \pm 100$  cts/s corresponding to a voltage spread of  $\pm 3$  mV. This is still a very homogeneous distribution, which—if at all—shows hardly any similarities with Fig. 3 (right).

It is also noteworthy that the difference in the luminescence intensity (1900 versus 900 cts/s) between both images in Fig. 4 corresponds to the voltage difference of ~20 mV being in a good agreement with the voltage difference observable in Fig. 1.

This proves in addition to the TLM analysis clearly that series resistance has severely degraded dragging along the fill factor in Fig. 2. Such a kind of contact resistance degradation at elevated temperatures in the range 200–300 °C has been observed before [45]. In addition, it was recently reported that annealing steps exceeding 400 °C lead to a degradation of contact resistance as well [46], [47].

However, this alone cannot explain consistently why  $V_{\text{oc}}$  and  $j_{\text{sc}}$  drop as well, because under  $V_{\text{oc}}$  conditions there should



not flow any current density  $j$  across the series resistance  $R_s$ , and therefore, internal (pn-junction) voltage  $V_{\text{int}}$  and external voltage  $V_{\text{ext}} = V_{\text{int}} + j \cdot R_s$  will concur—at least if the sample is laterally homogeneous regarding the diode properties. Lateral inhomogeneity (in diode's saturation current density) will cause compensation currents between different cell regions and can cause external voltage drops; however, this was not observed here (see Fig. 4).

So it can be concluded that there are at least two effects at work: A degradation of series resistance plus a second “internal” component responsible for the observed degradation in  $V_{\text{oc}}$  and  $j_{\text{sc}}$ . Whether these two effects are correlated after all and feature the same origin will be discussed after the following detailed root cause analysis.

### B. Possible Candidates for the “Internal” Component

Generally speaking, there are multiple ways to change  $V_{\text{oc}}$  and  $j_{\text{sc}}$  of a solar cell (measured according to STC [35]). The dependencies of  $V_{\text{oc}}$  can be described by the well-known two diode system, which links current density  $j$  and external voltage  $V_{\text{ext}} = V_{\text{int}} + j \cdot R_s$  [48]

$$j(V_{\text{ext}}) = j_{01} \cdot \left[ \exp \left( \frac{qV_{\text{int}}}{n_1 kT} \right) - 1 \right] + j_{02} \cdot \left[ \exp \left( \frac{qV_{\text{int}}}{n_2 kT} \right) - 1 \right] - j_{\text{ph}} \quad (2)$$

introducing the saturation current densities  $j_{01}$  and  $j_{02}$ , as well as the diode's ideality factors  $n_1 = 1$  and  $n_2 = 2$ . Furthermore,  $q$  represents the elementary charge,  $k$  Boltzmann's constant, and  $T$  the absolute temperature. A parallel resistance component is deliberately neglected here as it was found to be sufficiently high ( $\gg 50 \text{ k}\Omega \cdot \text{cm}^2$ ) as to impact FF noticeably and it does not differ significantly between nondegraded and degraded case.  $V_{\text{oc}}$  follows from the condition  $j(V_{\text{ext}}) = 0$  implying  $V_{\text{ext}} = V_{\text{int}} = V_{\text{oc}}$ .

The approximation that  $j_{\text{ph}}$  equals  $j_{\text{sc}} = j(V_{\text{ext}} = 0)$  might be questionable with regard to the massively increased series resistance so that the observed loss in  $j_{\text{sc}}$  in Fig. 1 might be—at least in parts—a consequence of the series resistance increase. In principle, a certain area of the solar cell could be virtually decoupled from global current extraction due to the high series resistance because the current flow results in such a high voltage drop that the photogenerated charge carriers more likely recombine locally than participate in global current extraction. Whether this is the case in the degraded sample can be proven by photoluminescence imaging under short-circuit conditions. If a certain region decouples from global current extraction, local voltage rises (up to  $V_{\text{oc}}$ ) and, in consequence, luminescence intensity will increase according to (1). Fig. 5 shows a photoluminescence image of both the nondegraded (left) and the degraded (right) subsample in Figs. 3 and 4. Both show a homogeneous signal on an extremely low level without any regions decoupling from current extraction indicating that  $j_{\text{sc}}$  is efficiently extracted even in the degraded sample and that the loss in  $j_{\text{sc}}$  is not related to the series resistance increase.

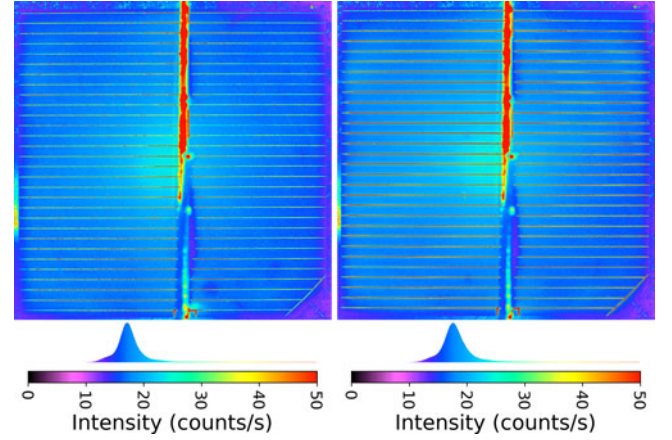


Fig. 5. Short-circuit photoluminescence images including intensity histograms taken at  $\sim 1$  sun (photon flux equivalent [34], 808 nm laser illumination,  $25^\circ\text{C}$ ) of the same nondegraded (left) and a degraded (right)  $5 \text{ cm} \times 5 \text{ cm}$  subsample, as in Fig. 3. The intense feature above the front busbar is an artifact caused by the excitation light reflected at the mounting of the contacting setup only becoming visible due to the overall low level of luminescence intensity.

Even though the massively increased series resistance ( $\sim 8 \Omega \cdot \text{cm}^2$ ) noticeably distorts the  $j(V)$  characteristic, it is still “too low” to measurably reduce  $j_{\text{sc}}$ . Hence, photogenerated current density  $j_{\text{ph}}$  can in the following be approximated by  $j_{\text{sc}}$ .

The saturation current density  $j_{01}$  can be split up in a base component  $j_{0b}$  and an emitter component  $j_{0e}$ , and the base component is given by the saturation current density of a finite diode [43], [44]

$$j_{01} = j_{0e} + j_{0b} = j_{0e} + qn_i^2 \frac{D}{N_{\text{dop}} \cdot L_{\text{eff}}} \quad (3)$$

introducing, amongst the (p-type) doping level  $N_{\text{dop}}$ , the minority carrier (electron) diffusion constant  $D$  and the intrinsic carrier concentration  $n_i$ , and the effective diffusion length  $L_{\text{eff}}$ , which accounts for recombination at the rear surface described by the surface recombination velocity  $S_R$  [43], [44]

$$L_{\text{eff}} = L \cdot \left[ 1 + \frac{S_R \cdot L}{D} \cdot \tanh \left( \frac{w}{L} \right) \right] / \left[ \frac{S_R \cdot L}{D} + \tanh \left( \frac{w}{L} \right) \right] \quad (4)$$

and which differs from the diffusion length  $L = (D \cdot \tau)^{1/2}$  determined by bulk lifetime  $\tau$  (including the defect-limited bulk lifetime  $\tau_b$  and all other recombination channels) if  $L$  comes close to or surpasses the base thickness  $w$ . Note that in the following, the defect-limited bulk lifetime  $\tau_b$  was chosen deliberately for the description of lifetime as it scales directly with defect density and, in contrast to the bulk lifetime  $\tau$ , it is not impacted by intrinsic recombination mechanisms.

Thus,  $V_{\text{oc}}$  finally depends on four entities: defect-limited bulk lifetime  $\tau_b(\Delta n)$ , rear surface recombination velocity  $S_R(\Delta n)$ , emitter saturation current density  $j_{0e}$ , and saturation current density  $j_{02}$ , which is typically identified with recombination in the space charge region (SCR). Besides these factors, it depends also on  $j_{\text{sc}} (\sim j_{\text{ph}})$ .

In principle,  $j_{0e}$  is describable in a similar manner as  $j_{0b}$ ; however, the situation is more complicated as the  $n^+$  emitter formed by phosphorous in-diffusion features, on the one hand, a varying

doping profile in depth and, on the other hand, a nonconstant charge carrier lifetime and diffusivity in depth due to the doping profile (Auger limitation) and other defects originating from the diffusion. Nevertheless, it can be calculated numerically, when doping profile and charge carrier lifetime are given.

The dependencies of  $j_{sc}$  are a bit more complicated to describe. Generally speaking,  $j_{sc}$  corresponds to the convolution of depth- and wavelength-dependent generation  $G(\lambda, z)$  and depth-dependent collection probability  $\psi(z)$  [44]

$$\begin{aligned} j_{sc} &= q \cdot \int_{\lambda_1}^{\lambda_2} \int_0^w \psi(z) \cdot G(\lambda, z) d\lambda dz \\ &= q \cdot \int_{\lambda_1}^{\lambda_2} \text{IQE}(\lambda) \cdot (1 - R(\lambda)) \cdot \phi(\lambda) d\lambda. \end{aligned} \quad (5)$$

Based on the reciprocity theorem of Donolato [49], the collection probability  $\psi_b(z)$  in the base of a solar cell with a front-side emitter ( $z = 0$ , neglecting its actual finite thickness) can be described by [44]

$$\psi_b(z; w, L_{\text{eff}}) = \cosh\left(\frac{z}{L}\right) - \frac{L}{L_{\text{eff}}} \cdot \sinh\left(\frac{z}{L}\right) \quad (6)$$

where  $L_{\text{eff}}$  is the same effective diffusion length introduced in (4).  $\psi_b(z)$  decreases with increasing distance to the pn-junction as it is less likely to collect a minority charge carrier further away. In principle, the same accounts for the collection in the emitter as well; however, again the situation is complicated by the nonconstant doping profile, but  $\psi_e$  can be calculated numerically.

Generation  $G(\lambda, z)$  itself is the product of incident photon flux  $\phi(\lambda)$  and an optical component  $\Omega(\lambda, z; w)$ , which describes how incoming light is partially reflected (reflection  $R(\lambda)$ ) and partially coupled into the device ( $1 - R(\lambda)$ ), and then subsequently absorbed, internally reflected, and scattered.  $\Omega$  is explicitly responsible for the generated charge carrier density at a certain depth  $z$ , and therefore, its exact mathematical formulation is linked closely to the evaluation of collection probability. In consequence, an inexact description of  $\Omega$  will result in an inaccurate evaluation of the collection probability  $\psi_b(z)$  or internal quantum efficiency IQE( $\lambda$ ) [defined by (5)]. Note that the measured  $\text{IQE}_{\text{meas}} = \text{IQE} \times sf$  may deviate from the true IQE by a global scaling factor  $sf$  due to the measurement principle [44].

Thus,  $j_{sc}$  depends—as  $V_{oc}$  does—via  $L_{\text{eff}}$  on defect-limited bulk lifetime  $\tau_b(\Delta n)$  and rear surface recombination velocity  $S_R(\Delta n)$ . In addition,  $j_{sc}$  depends on the recombination in the emitter. Even though it is from a mathematical point of view difficult to link the saturation current density  $j_{0e}$  to the short-circuit current density  $j_{sc}$ , it seems obvious that introducing additional recombination within the emitter will increase  $j_{0e}$  and decrease  $j_{sc}$ .

However, the analytical approach described above is strictly valid only in a perfectly one-dimensional scenario. The used PERC-type solar cells in this experiment feature at least a two-dimensional domain due to their contact structure. Therefore, at least the entities  $j_{0e}$  and  $S_R$  in the experiment are to be

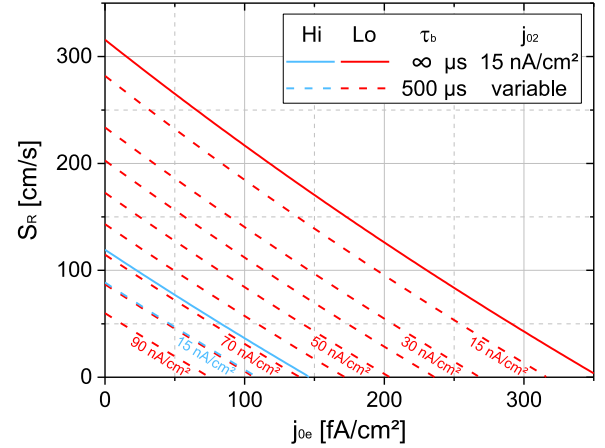


Fig. 6. Iso- $V_{oc}$  curves in dependence of emitter saturation current density  $j_{0e}$  and rear surface recombination velocity  $S_R$  with varying saturation current density  $j_{02}$  and defect-limited bulk lifetime  $\tau_b$ . Blue lines mark a nondegraded “Hi” –  $V_{oc}$  of  $\sim 670$  mV, while red lines mark a degraded “Lo” –  $V_{oc}$  of  $\sim 649$  mV.

understood as effective values being a blend of noncontacted and contacted areas.

Generally speaking, a deterioration of all the mentioned entities (alone or combined) will lead to a degradation of  $V_{oc}$  and/or  $j_{sc}$  and the fundamental question is if a certain degree of deterioration is consistent with the observed data. In the following, the influence of each of these entities is evaluated by simulation and collated with observation.

### C. Degradation Within the Space Charge Region?

A defect formation within the SCR, e.g., due to metal contamination underneath the contact regions, would appear as an increase in  $j_{02}$  in (2). From fitting the two-diode model (2) to the nondegraded “Hi”- $j(V)$  curve, it is concluded that  $j_{02, \text{Hi}}$  is  $\sim 15$  nA/cm<sup>2</sup>. Assuming a certain bulk lifetime  $\tau_b$  limited by defect-driven recombination, one can numerically calculate the iso- $V_{oc}$   $S_R(j_{0e}; j_{02}, \tau_b)$  curves from (2) shown in Fig. 6 dependent on emitter saturation current density  $j_{0e}$  with respect to varying SCR saturation current density  $j_{02}$ . The solid blue line marks an upper limit for the  $S_{R, \text{Hi}}(j_{0e})$  relation for the nondegraded “Hi”- $V_{oc}$  of  $\sim 670$  mV taking no SRH limitation (meaning only Auger-limitation;  $\tau_b = \infty$ ) into account. If  $\tau_b$  is defect-limited to  $500 \mu\text{s}$  (the validity of this assumption will be discussed later on), the actual  $S_{R, \text{Hi}}(j_{0e})$  relation (dash-dotted blue line) is shifted to lower values meaning additional losses in the bulk have to be compensated by less losses in the emitter and at the rear surface. For these blue lines,  $j_{02, \text{Hi}}$  of  $15$  nA/cm<sup>2</sup> was assumed.

The degraded “Lo” –  $V_{oc}$  of  $\sim 649$  mV yields the iso- $V_{oc}$   $S_{R, \text{Lo}}(j_{0e})$  curves in red assuming again  $\tau_b$  of  $500 \mu\text{s}$ . If also  $j_{02}$  remains unchanged, the additional losses in  $V_{oc}$  have to result from an increase in  $S_R$  and/or  $j_{0e}$ , or in other words, the iso- $V_{oc}$   $S_{R, \text{Lo}}(j_{0e})$  curve shifts to higher values. However, if neither  $S_R$  nor  $j_{0e}$  increases,  $S_{R, \text{Hi}}(j_{0e}; j_{02, \text{Hi}})$  and  $S_{R, \text{Lo}}(j_{0e}; j_{02, \text{Lo}})$  have to match and losses have to originate from an increase in  $j_{02}$  instead. Fig. 6 illustrates that  $j_{02, \text{Lo}}$  has to increase (from  $j_{02, \text{Hi}}$

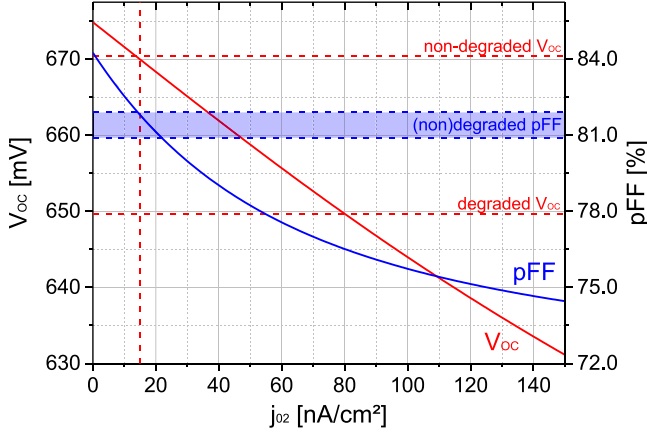


Fig. 7. Calculated  $V_{oc}$  (red) and pFF (blue) in dependence of  $j_{02}$ .

$\sim 15 \text{ nA/cm}^2$  in the nondegraded case) to at least  $70 \text{ nA/cm}^2$  or more likely to more than  $80 \text{ nA/cm}^2$  to explain the observed  $V_{oc}$  loss.

However, an increase in  $j_{02}$  would also change the pFF as it is demonstrated in Fig. 7. An increase to  $\sim 75 \text{ nA/cm}^2$  would result in a drop of pFF to  $\sim 77\%$ , which is not consistent with the observed pFF of  $\sim 81\%$ . More precisely, even a slight increase in  $j_{02}$  should result in a noticeable decrease in pFF. It can, therefore, be concluded that the questionable internal degradation component is most probably not linked to an increase in  $j_{02}$  interpretable as defect formation in the SCR.

#### D. Degradation Within the Emitter?

The observed degradation might alternatively result from a defect formation in the emitter region, e.g., by in-diffusion of a contaminant from the passivation layer. PC1D mod 6.2 [50]–[52] was used to evaluate this hypothesis. Even though in-diffusion of a contaminant would likely result in a characteristic depth-dependent profile, it was in the following assumed that—in order to simplify the scenario—a homogeneous defect-rich layer of  $100 \text{ nm}$  featuring a certain defect-related lifetime  $\tau_e$  occurs underneath the surface. It should be noted that the effective lifetime in this defect-rich layer within the emitter is then determined by defect-related as well as Auger-related recombination. The latter is quite strongly limiting the effective lifetime due to the high doping level; thus,  $\tau_e$  has to drop to the ns-range to take effect. The simulated cell corresponds to the “Hi”- $V_{oc}$  level in the absence of the defect-rich layer. The simulation results are shown in Fig. 8. While  $j_{sc}$  drops with decreasing lifetime  $\tau_e$  in the defect-rich layer,  $j_{0e}$  increases concurrently, and the observed loss in  $j_{sc}$  concurs with an increase of  $j_{0e}$  to  $\sim 280 \text{ fA/cm}^2$  applying the spectrum of the used flash IV-tester (taken from [38]). Note that  $j_{sc}$  would differ slightly if sun’s spectrum (ASTM G173 [36]) according to STC [35] would have been used. The effect of different spectra will be discussed in the context of Fig. 10.

Using (2)–(4), a set of iso- $V_{oc}$   $S_R(\tau_b; j_{0e})$  curves with varying  $j_{0e}$  were calculated for the “Hi”- $V_{oc}$  and “Lo”- $V_{oc}$  level, as shown in Fig. 9. As before, additional  $j_{0e}$  losses need to be compensated by less losses in other parts of the solar cell

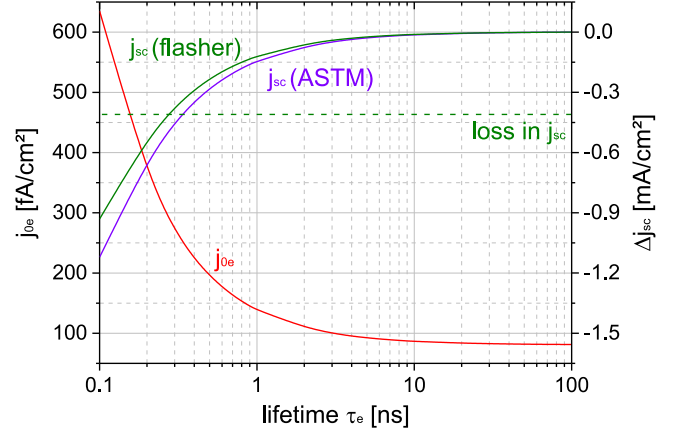


Fig. 8. Loss in  $j_{sc}$  and  $j_{0e}$  in dependence of the defect-limited lifetime  $\tau_e$  in a defect-rich  $100 \text{ nm}$  layer in the emitter.

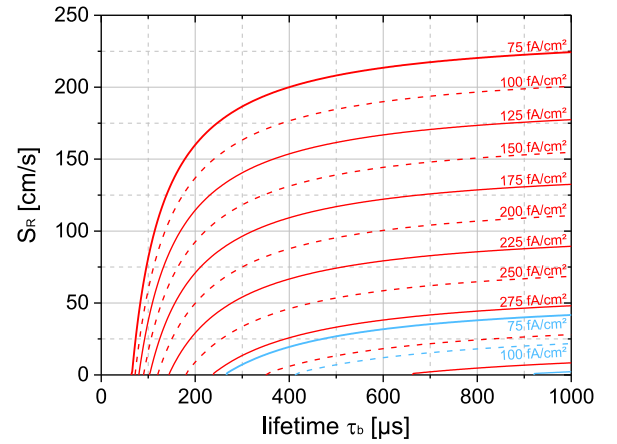


Fig. 9. Iso- $V_{oc}$  curves in dependence of defect-limited bulk lifetime  $\tau_b$  and rear surface recombination velocity  $S_R$  with varying emitter saturation current density  $j_{0e}$ . Blue lines mark a nondegraded “Hi”- $V_{oc}$  of  $\sim 670 \text{ mV}$ , red lines mark a degraded “Lo”- $V_{oc}$  of  $\sim 649 \text{ mV}$ .

to maintain the same  $V_{oc}$ . Thus, increasing  $j_{0e}$  leads to a shift of the  $S_R(\tau_b; j_{0e})$  curves to lower  $S_R$  values. From Fig. 6, it seems reasonable to assume that the nondegraded emitter (blue lines) exhibits  $j_{0e,Hi}$  of  $\sim 75 \text{ fA/cm}^2$ , which restricts  $S_R$  and  $\tau_b$  to a reasonable range for the “Hi”- $V_{oc}$  level. If neither  $S_R$  nor  $\tau_b$  changes during the observed degradation,  $j_{0e,Lo}$  has to be adapted so that  $S_{R,Lo}(\tau_b; j_{0e,Lo})$  (red lines) matches  $S_{R,Hi}(\tau_b; j_{0e,Hi})$  (blue lines). This is the case for  $j_{0e,Lo}$  being in the range of  $\sim 280 \text{ fA/cm}^2$ , which is more or less the value from the PC1D simulation mentioned above (see Fig. 8).

In other words, the increase of  $j_{0e}$  to  $\sim 280 \text{ fA/cm}^2$  due to defect formation in the emitter could consistently reproduce both the observed  $V_{oc}$  and  $j_{sc}$  losses. In addition, pFF would remain rather unchanged in the observed  $81\text{--}82\%$  range.

The loss in  $j_{sc}$  due to the formation of a defect-rich layer in the emitter should leave its mark in the  $\text{IQE}(\lambda)$  of short wavelength (UV) light that is totally or at least to a large fraction absorbed within the emitter. Fig. 10 shows a selection of  $\text{IQE}(\lambda)$  curves with varying  $\tau_e$  used for the  $j_{sc}$  calculation in the above-mentioned PC1D simulation (see Fig. 8). The nondegraded “Hi”-case corresponds to around  $10 \text{ ns}$  or above, where



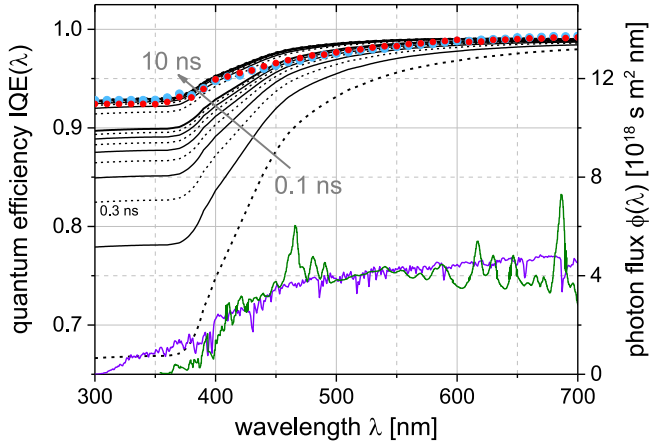


Fig. 10. Internal quantum efficiency IQE versus wavelength  $\lambda$ . The array of black lines marks simulation results with varying  $\tau_e$  from 0.1 to 10 ns. In addition, measured data (using bias light of  $\sim 1/3$  sun) of the nondegraded (blue) and degraded (red) sample are shown. Furthermore, spectral photon flux of the ASTM G173 (violet [36]) and the used flasher system (green [38]) is given.

a further increase in  $\tau_{e,Hi}$  is irrelevant, while Fig. 8 suggests a degraded  $\tau_{e,Lo}$  of  $\sim 0.3$  ns. Thus, it can be concluded that, due to degradation within the emitter, an IQE difference of  $\sim 0.1$  between degraded IQE<sub>Lo</sub> and nondegraded IQE<sub>Hi</sub> should be observable in the range up to 350 nm closing gradually toward 600 nm. Such a 0.1 gap in IQE should be easily detectable.

However, the measurements using a LOANA tool from pv-tools in the nondegraded (blue) and degraded (red) case depicted in Fig. 10 do not show any gap in the short wavelength regime. Thus, it can be concluded that the observed  $j_{sc}$  loss is not due to defect formation in the noncontact regions of the emitter and has a different origin. For the loss in  $V_{oc}$ , the situation is more complicated, as  $j_{0e}$  is always a blend of the noncontacted and contacted regions of the emitter. If  $j_{0e}$  underneath an emitter contact increases, it would probably not cause a severe loss in  $j_{sc}$ , but nevertheless cause a loss in  $V_{oc}$ .

Also shown in Fig. 10 are photon flux spectra of the ASTM G173 (STC, AM 1.5 g [36]) and of the flasher system [38] used to determine  $j_{sc}$  in this experiment. It should be noted that even though the system is AAA-rated [37], it features hardly any intensity in the UV-range below 350 nm, making it partially blind toward changes in the short wavelength IQE( $\lambda$ ) [53]. This is the reason for the slight discrepancy in  $j_{sc}$  loss (green versus violet) in Fig. 8.

#### E. Degradation in the Base?

Defect formation in the base of the solar cell will result in a reduction of defect-limited bulk lifetime  $\tau_b$ . Fig. 11 shows  $V_{oc}$  (numerically) calculated from (2)–(4) in dependence of  $S_R$  and  $\tau_b$  with fixed  $j_{0e}$  (75 fA/cm<sup>2</sup>) and  $j_{02}$  (15 nA/cm<sup>2</sup>). Note that both  $S_R(\Delta n)$  and  $\tau_b(\Delta n)$  can depend on the injection level  $\Delta n$ , which is linked to  $V_{oc}$  via (1).  $S_R$  and  $\tau_b$  in Fig. 11 are, therefore, to be understood as actual values at whatever injection level is present at  $V_{oc}$  if any injection dependence exists at all. Also marked in Fig. 11 are iso- $V_{oc}$  curves for the degraded “Lo” –  $V_{oc}$  ( $\sim 649$  mV, black) and nondegraded

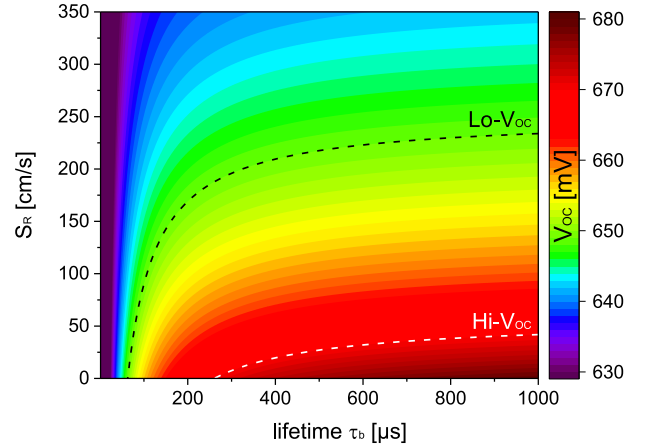


Fig. 11. Contour plot of  $V_{oc}$  in dependence of defect-limited bulk lifetime  $\tau_b$  and rear surface recombination velocity  $S_R$ .

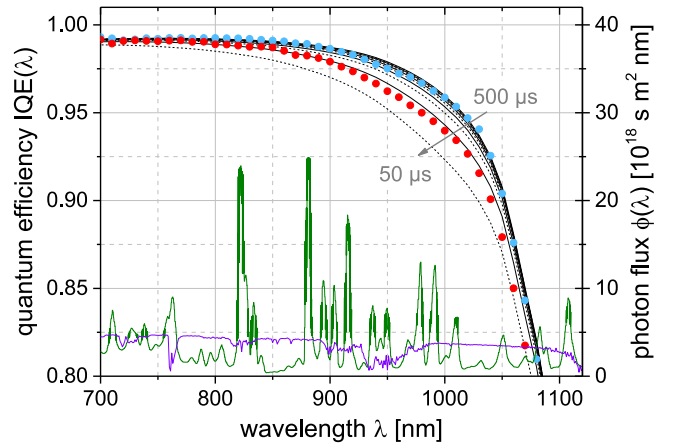


Fig. 12. Internal quantum efficiency IQE versus wavelength  $\lambda$ . The array of black lines marks simulation results with varying  $\tau_b$  from 50 to 500  $\mu s$  in 50  $\mu s$  steps and fixed  $S_R$  of 30 cm/s. In addition, measured IQE( $\lambda$ ) (using bias light of  $\sim 1/3$  sun) of the nondegraded (blue) and degraded (red) sample are shown. Furthermore, spectral photon flux of the ASTM G173 (violet [36]) and of the used flasher system (green [38]) is given.

“Hi” –  $V_{oc}$  ( $\sim 670$  mV, white) case. The latter white curve also sets an upper limit for  $S_R$  ( $< 40$  cm/s) and a lower limit for  $\tau_b$  ( $> 250$   $\mu s$ ) if one of these entities is not changing during the observed degradation. As can be seen, either  $S_R$  and/or  $\tau_b$  has to change noticeably to explain the loss in  $V_{oc}$ . Degradation of  $\tau_b$  corresponds to a horizontal cut line, and—virtually irrespective of the (nondegrading)  $S_R$  value— $\tau_{b,Lo}$  has to drop as low as 75  $\mu s$  to reproduce the observed  $V_{oc}$  loss. That this degraded defect-limited lifetime is quite realistic shows the comparison with BO-LID, where bulk lifetime can drop even to the single digit  $\mu s$ -range with an unfavorable combination of high boron doping and high oxygen contamination level [6].

Such strong reduction in  $\tau_b$  should also leave its mark in the long wavelength IQE( $\lambda$ ) as IR light of, e.g.,  $\sim 1000$  nm features an absorption length ( $L_{abs} \sim 160$   $\mu m$ ) comparable to the solar cell thickness (145  $\mu m$ ), and thus generates excess charge carriers close to the rear surface and far from the pn-junction at the front side. Fig. 12 shows an array of IQE( $\lambda$ ;  $\tau_b$ ) curves (black lines) with varying  $\tau_b$  and fixed  $S_R = 30$  cm/s calculated with the

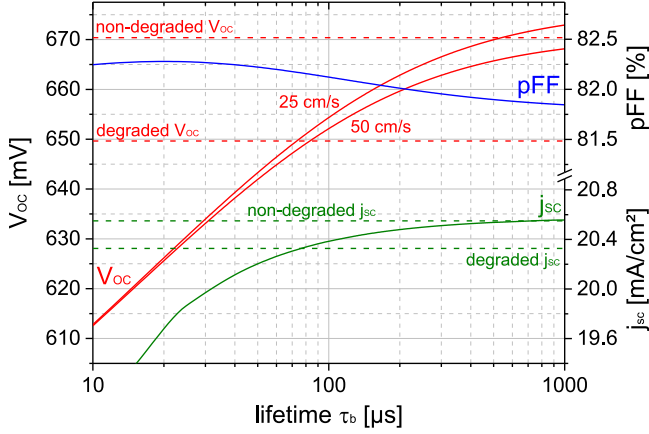


Fig. 13. Calculated dependence of  $V_{oc}$ ,  $j_{sc}$ , and pFF on defect-related bulk lifetime  $\tau_b$ .

program Lassie [54] (using the optical model of IQE-1D [55]). With decreasing  $\tau_b$ , a gap between the  $\text{IQE}(\lambda; \tau_b)$  curves arises; however, the exact shape of the calculated  $\text{IQE}(\lambda; \tau_b)$  curve depends on the optical modeling meaning  $\Omega(\lambda, z; w)$  as introduced before.

The measured data (scaled to their measured  $j_{sc}$ ) of the non-degraded (blue) and degraded (red) case in Fig. 12 show such a gap that could indeed result from a reduction of  $\tau_b$ . Unfortunately, quantitative evaluation of  $L_{eff}$  (and thus  $\tau_b$  with known  $S_R$ ) from the measured data has proven unreliable as the exact values correlate strongly with the optical modeling parameters and the steeper descent of the measured data compared to the simulated curves above 1050 nm suggests a deficiency of the optical modeling.

Based on the dependencies of  $V_{oc}$  (see Fig. 11) and  $\text{IQE}(\lambda)$  (see Fig. 12) on defect-limited bulk lifetime  $\tau_b$ , the consistency of  $V_{oc}$  and  $j_{sc}$  losses can be evaluated, as shown in Fig. 13. A defect-limited lifetime  $\tau_b$  of  $\sim 500 \mu\text{s}$  or above in the non-degraded state seems reasonable taking  $V_{oc}$  into account and  $S_R$  in the range of 25–50 cm/s. For the degraded case, the exact value of  $S_R$  makes hardly a difference,  $\tau_b$  would have to drop to  $\sim 75 \mu\text{s}$ . As the optical modeling is critical above 1050 nm, the loss in  $j_{sc}$  is only calculated in the spectral range of 700–1025 nm from Fig. 12 using the flasher spectrum (green [38]). In order to explain the loss in  $j_{sc}$ ,  $\tau_b$  would have to drop to  $\sim 75 \mu\text{s}$  as well. However, the predicted loss in  $j_{sc}$  exhibits a hard-to-estimate uncertainty due to the deficiency in optical modeling, and the almost perfect match in required lifetime should not be overstated.

In summary, a degradation of bulk lifetime could consistently explain the observed losses in  $V_{oc}$  and  $j_{sc}$  taking the  $j(V)$  and  $\text{IQE}(\lambda)$  results into account.

#### F. Degradation of Rear Surface Passivation?

Rear surface passivation is a blend of locally Al-doped contacted areas with high/low-junction field effect passivation and noncontacted areas with dielectric passivation. The latter relies on a mix of chemical passivation at the interface (low interface density of states in the bandgap) and a field effect passivation

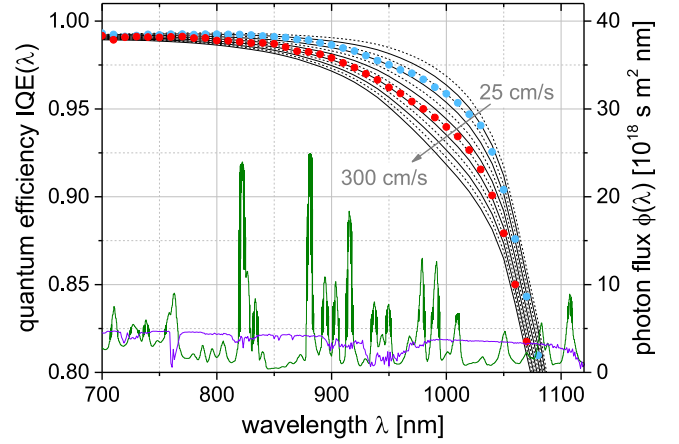


Fig. 14. Internal quantum efficiency  $\text{IQE}$  versus wavelength  $\lambda$ . The array of black lines marks simulation results with varying  $S_R$  from 25 to 300 cm/s in 25 cm/s steps and fixed  $\tau_b$  of 500  $\mu\text{s}$ . In addition, measured  $\text{IQE}(\lambda)$  (using bias light of  $\sim 1/3$  sun) of the nondegraded (blue) and degraded (red) are shown. Furthermore, spectral photon flux of the ASTM G173 (violet [36]) and the used flasher system (green [38]) is given.

due to fixed charges in the dielectric layer (stack). Both, the formation of new interface defect states and the loss in fixed charges would result in a deterioration of passivation quality and, in consequence, an increase in rear surface recombination velocity  $S_R$ .

Fig. 11 already showed that, besides a degradation of defect-related bulk lifetime  $\tau_b$ , a degradation of  $S_R$  could explain the observed  $V_{oc}$  loss as well. In this case, degradation would mean a vertical cut line in Fig. 11 and, assuming  $\tau_b \sim 500 \mu\text{s}$ ,  $S_{R,Lo}$  would have to increase to  $\sim 225$  cm/s. Even if  $\tau_b$  is considerably higher, the required  $S_{R,Lo}$  would hardly change.

As for the degradation of  $\tau_b$  discussed before, a degradation of  $S_R$  should leave its mark in the long wavelength  $\text{IQE}(\lambda)$  regime as well. Fig. 14 shows an array of  $\text{IQE}(\lambda; S_R)$  curves (black lines) with varying  $S_R$  and fixed  $\tau_b = 500 \mu\text{s}$  calculated with the program Lassie [54] (using the optical model of IQE-1D [55]). The resemblance of Figs. 12 and 14 is striking. At least on a high lifetime level, the influence of  $\tau_b$  and  $S_R$  is virtually indistinguishable as both determine  $L_{eff}$ , which, in turn, determines the collection probability  $\psi_b(z)$ .

Based on the dependencies of  $V_{oc}$  (see Fig. 11) and  $\text{IQE}(\lambda)$  (see Fig. 14) on  $S_R$ , the consistency of  $V_{oc}$  and  $j_{sc}$  losses can be evaluated, as shown in Fig. 15. Again, only the spectral range of 700–1025 nm was used. Both losses in  $V_{oc}$  and  $j_{sc}$  can be consistently explained by an increase of  $S_R$  to 175–225 cm/s. Again, the predicted loss in  $j_{sc}$  exhibits a hard-to-estimate uncertainty due to the deficiency in optical modeling and the discrepancy in required  $S_R$  should not be overstated.

In summary, a degradation of rear surface passivation could also consistently explain the observed losses in  $V_{oc}$  and  $j_{sc}$  taking the  $j(V)$  and  $\text{IQE}(\lambda)$  results into account.

#### G. Bulk or Rear Surface Passivation?

As shown above, a degradation of bulk lifetime  $\tau_b$  and rear surface recombination velocity  $S_R$  is hardly distinguishable on



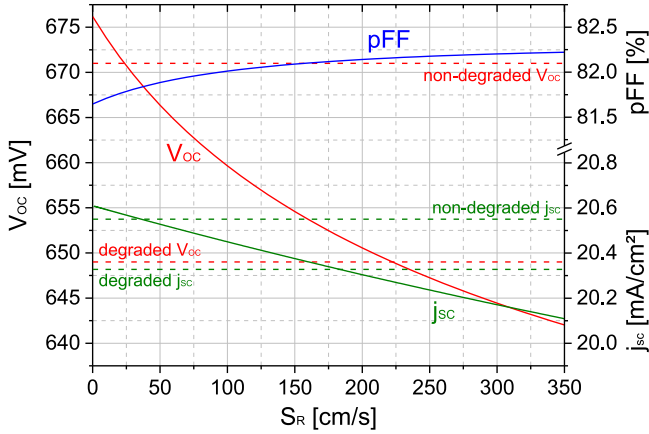


Fig. 15. Calculated dependence of  $V_{oc}$ ,  $j_{sc}$ , and pFF on rear surface recombination velocity  $S_R$  using a fixed bulk lifetime  $\tau_b$  of 500  $\mu s$ .

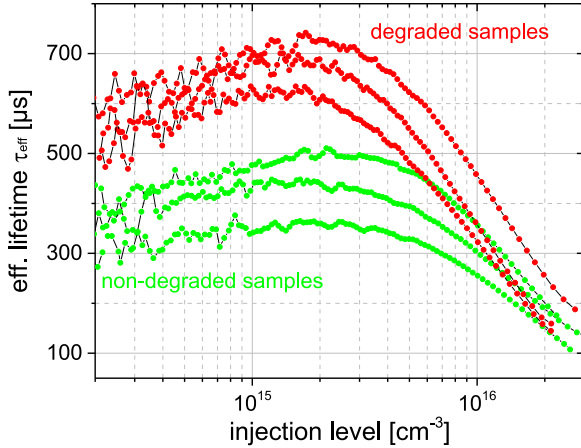


Fig. 16. Measured injection-dependent effective lifetime of the wet-chemically repassivated nondegraded and degraded sample (three subsamples each).

solar cell level. The only way to prove whether the first or the second effect is responsible for the observed degradation phenomenon is to assess bulk lifetime directly. For this purpose, the Ag (front) and Al (rear) metallization, the passivation layers, and the emitter of both the nondegraded and the degraded samples (three 5 cm  $\times$  5 cm subsamples each) were wet-chemically stripped/etched in HCl, aqua regia, and an acidic polishing solution consisting of acetic acid,  $HNO_3$ , and HF. Within this process, several micrometers were removed, especially due to the deep penetration of the Al-alloyed local rear contacts. Thereafter, the samples were oxidized in a solution of  $H_2O_2$  and  $H_2SO_4$  at elevated temperature ( $\sim 80^\circ C$ ) followed by an oxide etch in HF to remove residual contamination (Piranha clean). For the assessment of bulk lifetime, the surfaces were temporarily wet-chemically passivated by a 0.8 molar iodine/ethanol solution [56], [57] capable of revealing effective lifetimes up to  $\sim 1$  ms. However, passivation quality is known to be somewhat unreliable, and therefore, the effective lifetime of high bulk quality material is often only a lower limit for the true bulk lifetime. Fig. 16 shows the injection-dependent effective lifetime

$\tau_{eff}$  measured via a photoconductance decay technique [58], [59] (WCT 120 from Sinton Instruments, generalized mode).

Contrary to the expectations of  $\tau_{b,Hi}$  exceeding 500  $\mu s$  for the nondegraded sample and  $\tau_{b,Lo}$  being  $\sim 75 \mu s$  for the degraded sample at the injection level of  $\sim 7.5 \cdot 10^{14} cm^{-3}$  [corresponding to “Lo”- $V_{oc}$  of  $\sim 649$  mV according to (1)], measured lifetime behaves completely different. Measured effective lifetimes are even higher for the degraded sample (600–700  $\mu s$ ) than for the nondegraded sample (300–450  $\mu s$ ). This can be understood taking the recovery phase from BO-LID in Fig. 1 into account. The treatment of the nondegraded sample (green, Fig. 1) was broken off as it reached the intermediate maximum. However, the maximum is the result of the upward trend due to the recovery from BO-LID and the beginning of the downward trend of the second drop, meaning that the recovery from BO-LID was not complete at that point, and bulk lifetime as well as  $V_{oc}$  would have risen further if the second drop would not have occurred. With regard to the long treatment time of the degraded sample (red, Fig. 1), the recovery from BO-LID was most probably completed for this sample and the red data in Fig. 16 correspond to the BO-LID-free bulk lifetime.

Nevertheless, it cannot be excluded that the discrepancy in measured lifetime in Fig. 16 is at least in parts due to an inferior performance of the iodine/ethanol passivation on the nondegraded sample. In that case, measured lifetime has to be interpreted as a lower limit of the true bulk lifetime, and—as lifetimes are by far higher than  $\sim 75 \mu s$ —the observation is not consistent with the expectations.

One could argue that the sample preparation involving several minutes at  $\sim 80^\circ C$  without illumination might have seriously influenced the bulk lifetime and might have reversed the observed degradation. To exclude that possibility, another degraded subsample was treated in darkness at  $\sim 80^\circ C$  for a duration longer than the sample preparation took. No significant change in  $V_{oc}$  was measured afterward; therefore, a systematic error due to an unintentional reversal of degradation during sample preparation can be excluded.

So, taking not only the  $j(V)$  and  $IQE(\lambda)$  data, but also the  $\tau_{eff}$  data into account, a severe degradation of defect-limited bulk lifetime  $\tau_b$  as the dominant driving factor behind the observed degradation can be excluded as well.

#### H. Degradation at the Surface or Only Close to the Surface?

Even though all results point at a degradation of rear surface passivation or rear surface recombination velocity  $S_R$ , there are still a few different scenarios imaginable, which cannot be distinguished further with the available data. Generally speaking,  $S_R$  consists of two components: a high/low-junction field effect passivation at the rear contacts and a dielectric passivation in between, which relies on chemical passivation of the interface plus a field effect of fixed charges in the dielectric layer (stack). Thus, deterioration of dielectric passivation could either be due to defect formation at the interface or a neutralization of fixed charges.

There is one more imaginable possibility. Defect formation could not only occur at the interface, but also in a thin bulk

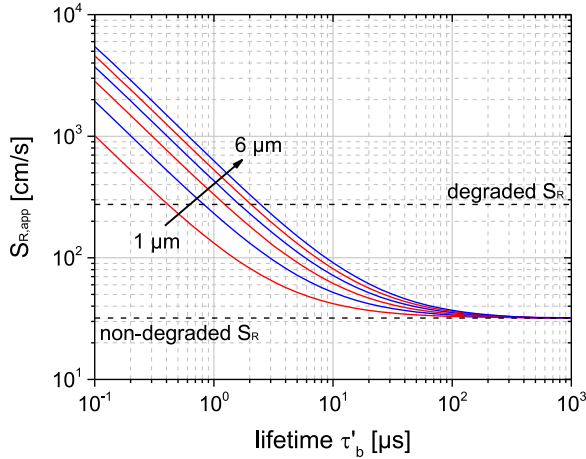


Fig. 17. Apparent rear surface recombination velocity  $S_{R,app}$  in dependence of defect-limited lifetime  $\tau'_b$  in a defect-rich layer of varying thickness underneath the physical surface.

region underneath the surface. Fig. 17 shows the results of a PC1D mod 6.2 [50]–[52] simulation in which a defect-rich layer of several micrometers with variable defect-limited lifetime  $\tau'_b$  was introduced underneath the dielectric passivation layer. The defect-rich layer leads to a deteriorated apparent  $S_{R,app}$  when  $\tau'_b$  in this layer is sufficiently low, even though the actual  $S_R$  has not changed. Note that a layer of several micrometers is by far thicker than the screening length of the fixed charges of the dielectric passivation layer.

For the lifetime measurement in Fig. 16, several micrometers had to be etched off to ensure a complete removal of the contact structure, especially on the rear side. It cannot be excluded that such a defect-rich layer was unintentionally removed.

Two different formation mechanisms of such a defect-rich layer are imaginable: 1) in-diffusion of a contaminant at low temperature (150 °C) or 2) activation of already existent defects that were introduced during (high temperature) solar cell processing. The latter defects could originate from plasma exposure during dielectric layer deposition or in-diffusion during the high-temperature firing step used for contact formation. For example, in-diffusing hydrogen could cause a defect-rich layer, as  $\text{SiN}_x\text{:H}$  layers deposited by plasma enhanced chemical vapor deposition (PECVD) can exhibit hydrogen concentrations in the range of  $10^{21} \text{ cm}^{-3}$  [60] resulting in extremely high hydrogen concentration in the silicon bulk at least close to the surface after the firing step [61]. As hydrogen solubility in pure silicon is by orders of magnitude lower, hydrogen tends to bind to impurities or to precipitate in the shape of platelets [62], [63], which both might represent a defect precursor, which is then activated during illuminated treatment. A similar discussion can be found in [32].

As mentioned in Section I, a surface-related degradation (SRD) was observed before, but only on lifetime samples [27], [32]. Fig. 18 shows a comparison of the  $V_{oc}$  data from Fig. 1 and lifetime data from a Cz-Si sample passivated by a PECVD-grown  $\text{SiO}_x/\text{SiN}_x\text{:H}$  stack, which was treated at 150 °C and 1 sun illumination intensity like the sample shown in Fig. 1. As can be seen, both samples exhibit similar features: a minimum I mainly caused by BO-LID, a maximum II resulting from the

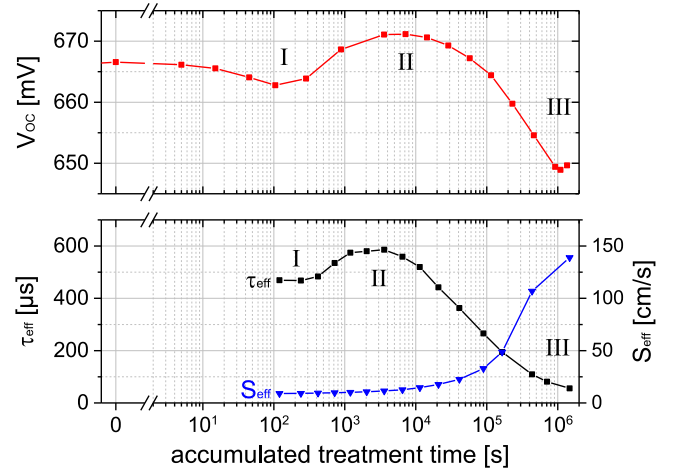


Fig. 18. Comparison of  $V_{oc}$  data in Fig. 1 (top) and lifetime data from a Cz-Si lifetime sample with  $\text{SiO}_x/\text{SiN}_x\text{:H}$  passivation stack (bottom). The shown surface recombination velocity  $S_{eff}$  was derived for better comparability from  $J_0$  values (determined as described in [32]). The roman numbers depict features according to [27] and [32].

recovery from BO-LID (regeneration) and beginning SRD, and a decline toward a minimum III due to SRD identifiable by rising values of the effective surface recombination velocity  $S_{eff}$ . Further details regarding SRD in lifetime samples can be found in [27] and [32].

Even though the  $\text{SiO}_x/\text{SiN}_x\text{:H}$  stack used for the lifetime sample is probably not identical to the stack in the investigated PERC-type solar cells (differing deposition conditions as well as firing conditions), it is noteworthy that the observed degraded  $S_{eff}$  values in Fig. 18 go well with the  $S_{R,Lo}$  values of the PERC cell (175–225 cm/s) taking into account the contribution of the inferior passivated local contacts and a surface enlargement of the nonplanar rear surface of the solar cell.

#### IV. CONCLUSION

Based on the analysis of  $j(V)$  data, a two-component degradation is likely. The first component involves a massive increase in series resistance originating from the contact resistance of the Ag fingers to the  $n^+$  emitter. No increase in contact resistance at the local Al-alloyed rear contacts was found. However, a rising series resistance cannot consistently explain  $V_{oc}$  and  $j_{sc}$  losses.

Only based on  $j(V)$  data, degradation by defect formation in either the emitter or the bulk or at the rear surface cannot be distinguished. All cases could consistently explain the observed  $V_{oc}$  and  $j_{sc}$  losses. Defect formation in the SCR can be excluded.

Together with short wavelength  $\text{IQE}(\lambda)$  data, a severe degradation in the noncontacted emitter region can be excluded. Even though a degradation underneath the contacted emitter regions could probably explain losses in  $V_{oc}$ , this would not consistently explain the observed losses in  $j_{sc}$ .

The analysis of long wavelength  $\text{IQE}(\lambda)$  data does not allow to distinguish between a degradation in the bulk or at the surface, at least not at a rather high lifetime level.

Only the combined analysis of  $j(V)$ ,  $\text{IQE}(\lambda)$ , and  $\tau_{eff}$  data after repassivation excludes a degradation in the deep bulk and

points at a degradation of the rear surface passivation. Whether this degradation takes place at the local rear contacts, at the c-Si-SiO<sub>x</sub>/SiN<sub>x</sub>:H interface (additional defect states), within the dielectric layers (loss of fixed charges), or within a thin defect-rich layer underneath the surface cannot be distinguished based on the available data.

A similar degradation was also found for a Cz-Si lifetime sample passivated by a PECVD SiO<sub>x</sub>/SiN<sub>x</sub>:H stack with respect to extent and timescale.

As the degradation of series resistance originates from the front-side contact resistance and the degradation of the “internal” component was located at the rear side of the sample, the two degradation components are probably not directly linked to each other. In addition, the onset of  $V_{oc}$  and  $j_{sc}$  degradation on the one hand (see Fig. 1) and FF degradation on the other hand (see Fig. 2) do not seem to precisely concur. Nevertheless, it cannot be fully excluded that both mechanisms are induced by the same trigger mechanism in the background and require a different threshold to become observable in the individual entities.

#### ACKNOWLEDGMENT

The authors would like to thank A. Schwarz, L. Mahlstaedt, J. Lindroos, and M. Hagner for technical support as well as F. Huster for constructive discussions on loss mechanisms in solar cells.

The content is the responsibility of the authors.

#### REFERENCES

- [1] F. Fertig *et al.*, “Mass production of p-type Cz silicon solar cells approaching average stable conversion efficiencies of 22%,” *Energy Procedia*, vol. 124, pp. 338–345, 2017.
- [2] International Technology Roadmap for Photovoltaic, ITRPV, 8th ed., 2017.
- [3] A. W. Blakers, A. Wang, A. M. Milne, J. Zhao, and M. A. Green, “22.8% efficient silicon solar cell,” *Appl. Phys. Lett.*, vol. 55, pp. 1363–1365, 1989.
- [4] H. Fischer and W. Pschunder, “Investigation of photon and thermal induced changes in silicon solar cells,” in *Proc. 10th IEEE Photovolt. Spec. Conf.*, Palo Alto, CA, USA, 1974, pp. 404–411.
- [5] S. W. Glunz, S. Rein, J. Y. Lee, and W. Warta, “Minority carrier lifetime degradation in boron-doped Czochralski silicon,” *J. Appl. Phys.*, vol. 90, pp. 2397–2404, 2001.
- [6] K. Bothe, R. Sinton, and J. Schmidt, “Fundamental boron-oxygen-related carrier lifetime limit in mono- and multicrystalline silicon,” *Prog. Photovolt., Res. Appl.*, vol. 13, pp. 287–296, 2005.
- [7] K. Bothe and J. Schmidt, “Electronically activated boron-oxygen-related recombination centers in crystalline silicon,” *J. Appl. Phys.*, vol. 99, 2006, Art. no. 013701.
- [8] A. Herguth, G. Schubert, M. Kaes, and G. Hahn, “A new approach to prevent the negative impact of the metastable defect in boron doped Cz silicon solar cells,” in *Proc. 3rd World Conf. Photovolt. Energy Conf.*, Waikoloa, HI, USA, 2006, pp. 940–943.
- [9] A. Herguth, G. Schubert, M. Käs, and G. Hahn, “Investigations on the long time behavior of the metastable boron-oxygen complex in crystalline silicon,” *Prog. Photovolt., Res. Appl.*, vol. 16, pp. 135–140, 2008.
- [10] A. Herguth and G. Hahn, “Kinetics of the boron-oxygen related defect in theory and experiment,” *J. Appl. Phys.*, vol. 108, 2010, Art. no. 114509.
- [11] S. Wilking, A. Herguth, and G. Hahn, “Influence of hydrogen on the regeneration of boron-oxygen related defects in crystalline silicon,” *J. Appl. Phys.*, vol. 113, 2013, Art. no. 194503.
- [12] S. Wilking, S. Ebert, A. Herguth, and G. Hahn, “Influence of hydrogen effusion from hydrogenated silicon nitride layers on the regeneration of boron-oxygen related defects in crystalline silicon,” *J. Appl. Phys.*, vol. 114, 2013, Art. no. 194512.
- [13] V. Voronkov and R. Falster, “The nature of boron-oxygen lifetime- degrading centres in silicon,” *Phys. Status Solidi C*, vol. 13, pp. 712–717, 2016.
- [14] T. Niewelt, J. Schön, W. Warta, S. W. Glunz, and M. C. Schubert, “Degradation of crystalline silicon due to boron-oxygen defects,” *IEEE J. Photovolt.*, vol. 7, no. 1, pp. 383–398, Jan. 2017.
- [15] J. Lindroos and H. Savin, “Review of light-induced degradation in crystalline silicon solar cells,” *Sol. Energy Mater. Sol. Cells*, vol. 147, pp. 115–126, 2016.
- [16] L. J. Geerligs and D. Macdonald, “Dynamics of light-induced FeB pair dissociation in crystalline silicon,” *Appl. Phys. Lett.*, vol. 85, pp. 5227–5229, 2004.
- [17] D. H. Macdonald, L. J. Geerligs, and A. Azzizi, “Iron detection in crystalline silicon by carrier lifetime measurements for arbitrary injection and doping,” *J. Appl. Phys.*, vol. 95, pp. 1021–1028, 2004.
- [18] D. Macdonald, J. Tan, and T. Trupke, “Imaging interstitial iron concentrations in boron-doped crystalline silicon using photoluminescence,” *J. Appl. Phys.*, vol. 103, 2008, Art. no. 073710.
- [19] C. Fahrland, Y. Ludwig, F. Kersten, and K. Petter, “Sponge LID - A new degradation mechanism?” in *Proc. 40th IEEE Photovolt. Spec. Conf.*, Denver, CO, USA, 2014, pp. 0135–0139.
- [20] K. Ramspeck *et al.*, “Light induced degradation of rear passivated mc-Si solar cells,” in *Proc. 27th Eur. Photovolt. Sol. Energy Conf.*, Frankfurt/Main, Germany, 2012, pp. 861–865.
- [21] F. Fertig, K. Krauß, and S. Rein, “Light-induced degradation of PECVD aluminium oxide passivated silicon solar cells,” *Phys. Status Solidi RRL*, vol. 9, pp. 41–46, 2015.
- [22] F. Kersten *et al.*, “Degradation of multicrystalline silicon solar cells and modules after illumination at elevated temperature,” *Sol. Energy Mater. Sol. Cells*, vol. 142, pp. 83–86, 2015.
- [23] K. Nakayashiki *et al.*, “Engineering solutions and root-cause analysis for light-induced degradation in p-type multicrystalline silicon PERC modules,” *IEEE J. Photovolt.*, vol. 6, no. 4, pp. 860–868, Jul. 2016.
- [24] D. Bredemeier, D. Walter, S. Herlufsen, and J. Schmidt, “Lifetime degradation and regeneration in multicrystalline silicon under illumination at elevated temperature,” *AIP Adv.*, vol. 6, 2016, Art. no. 035119.
- [25] C. Chan *et al.*, “Modulation of carrier-induced defect kinetics in multicrystalline silicon PERC cells through dark annealing,” *Solar RRL*, vol. 1, no. 2, 2017, Art. no. 1600028.
- [26] D. Chen *et al.*, “Evidence of an identical firing-activated carrier-induced defect in monocrystalline and multicrystalline silicon,” *Sol. Energy Mater. Sol. Cells*, vol. 172, pp. 293–300, 2017.
- [27] D. Sperber, A. Heilemann, A. Herguth, and G. Hahn, “Temperature and light induced changes in bulk and passivation quality of boron-doped float-zone silicon coated with SiN<sub>x</sub>:H,” *IEEE J. Photovolt.*, vol. 7, no. 2, pp. 463–470, Mar. 2017.
- [28] D. Sperber, A. Herguth, and G. Hahn, “A 3-state defect model for light induced degradation in boron-doped float-zone silicon,” *Phys. Status Solidi RRL*, vol. 11, 2017, Art. no. 1600408.
- [29] T. Niewelt *et al.*, “Light-induced activation and deactivation of bulk defects in boron-doped float-zone silicon,” *J. Appl. Phys.*, vol. 121, 2017, Art. no. 185702.
- [30] T. Niewelt *et al.*, “Understanding the light-induced degradation at elevated temperatures: Similarities between multicrystalline and float-zone p-type silicon,” *Prog. Photovolt., Res. Appl.*, to be published. doi: <https://doi.org/10.1002/pip.2954>.
- [31] D. Sperber, A. Herguth, and G. Hahn, “Investigating possible causes of light induced degradation in boron-doped float-zone silicon,” in *Proc. 33rd Eur. Photovolt. Sol. Energy Conf.*, Amsterdam, The Netherlands, 2017, pp. 565–568.
- [32] D. Sperber, A. Graf, D. Skorka, A. Herguth, and G. Hahn, “Degradation of surface passivation on crystalline silicon and its impact on light-induced degradation experiments,” *IEEE J. Photovolt.*, vol. 7, no. 6, pp. 1627–1634, Nov. 2017.
- [33] A. Herguth, C. Derricks, and G. Hahn, “Regeneration of boron-oxygen related degradation in Cz-Si PERC-type solar cells at high temperatures,” in *Proc. 33rd Eur. Photovolt. Sol. Energy Conf.*, Amsterdam, The Netherlands, 2017, pp. 557–560.
- [34] A. Herguth, “On the meaning (fullness) of the intensity unit ‘suns’ in light induced degradation experiments,” *Energy Procedia*, vol. 124, pp. 53–59, 2017.
- [35] *Photovoltaic Devices – Part 1: Measurement of Photovoltaic Current-Voltage Characteristics*, IEC Standard 60904-1, 1987.
- [36] *Photovoltaic Devices – Part 3: Measurement Principles for Terrestrial Photovoltaic (PV) Devices With Reference Spectral Irradiance Data*, IEC Standard 60904-3, 1989.



- [37] *Photovoltaic Devices – Part 9: Solar Simulator Performance Requirements*, IEC Standard 60904-9, 2007.
- [38] Cetus PV-Celltest 3, Manual, h.a.l.m. elektronik GmbH, 2013.
- [39] R. A. Sinton and A. Cuevas, "A quasi-steady-state open-circuit voltage method for solar cell characterization," in *Proc. 16th Eur. Photovolt. Sol. Energy Conf.*, Glasgow, U.K., 2000, pp. 1152–1155.
- [40] M. Wolf and H. Rauschenbach, "Series resistance effects on solar cell measurements," *Adv. Energy Convers.*, vol. 3, pp. 455–479, 1963.
- [41] H. H. Berger, "Contact resistance on diffused resistors," in *Proc. Digest Tech. Papers IEEE Int. Solid State Circuits Conf.*, Philadelphia, PA, USA, 1969, pp. 160–161.
- [42] H. Murrmann and D. Widmann, "Current crowding on metal contacts to planar devices," *IEEE Trans. Electron Devices*, vol. ED-16, no. 12, pp. 1022–1024, Dec. 1969.
- [43] M. Green, *Solar Cells: Operating Principles, Technology and System Applications*. Englewood Cliffs, NJ, USA: Prentice-Hall, 1982.
- [44] B. Fischer, *Loss Analysis of Crystalline Silicon Solar Cells Using Photoconductance and Quantum Efficiency Measurements*. Göttingen, Germany: Cuvillier Verlag, 2003.
- [45] A. Herguth and G. Hahn, "Temperature induced degradation of the contact resistance of Ag-screen printed p-type silicon solar cells," in *Proc. 24th Eur. Photovolt. Sol. Energy Conf.*, Hamburg, Germany, 2009, pp. 2012–2014.
- [46] A. Peral *et al.*, "Impact of extended contact cofiring on multicrystalline silicon solar cell parameters," *IEEE J. Photovolt.*, vol. 7, no. 1, pp. 91–96, Jan. 2017.
- [47] C. Chen *et al.*, "Instability of increased contact resistance in silicon solar cells following post-firing thermal processes," *Solar RRL*, vol. 1, 2017, Art. no. 1700129.
- [48] P. Würfel, *Physics of Solar Cells: From Principles to New Concepts*. Weinheim, Germany: Wiley VCH, 2005.
- [49] C. Donolato, "A reciprocity theorem for charge collection," *Appl. Phys. Lett.*, vol. 46, pp. 270–272, 1985.
- [50] PC1D mod 6.2. [Online]. Available: [www.pvlighthouse.com.au](http://www.pvlighthouse.com.au).
- [51] H. Haug, B. R. Olaisen, Ø. Nordseth, and E. S. Marstein, "A graphical user interface for multivariable analysis of silicon solar cells using scripted PC1D simulations," *Energy Procedia*, vol. 38, pp. 72–79, 2013.
- [52] H. Haug and J. Greulich, "PC1Dmod 6.2 – Improved simulation of c-Si devices with updates on device physics and user interface," *Energy Procedia*, vol. 92, pp. 60–68, 2016.
- [53] A. Herguth *et al.*, "Influence of spectral mismatch, cell reflection properties and IQE on the efficiency measurement," in *Proc. 26th Eur. Photovolt. Sol. Energy Conf.*, Hamburg, Germany, 2011, pp. 1555–1557.
- [54] Lassie, "QE evaluation software by PV-tools." [Online]. Available: [www.pv-tools.de](http://www.pv-tools.de).
- [55] R. Brendel and R. Plüner, "IQE1D– A computer program for routine quantum efficiency analysis," in *Proc. Tech. Digest 9th Int. Photovolt. Sci. Eng. Conf.*, Miyazaki, Japan, 1996, p. 521.
- [56] T. Horányi, T. Pavelka, and P. Tüttö, "In situ bulk lifetime measurements on silicon with a chemically passivated surface," *Appl. Surf. Sci.*, vol. 63, pp. 306–311, 1993.
- [57] N. E. Grant and J. D. Murphy, "Temporary surface passivation for characterisation of bulk defects in silicon: A review," *Phys. Status Solidi RRL*, vol. 11, 2017, Art. no. 1700243.
- [58] R. A. Sinton, A. Cuevas, and M. Stuckings, "Quasi-steady-state photoconductance, a new method for solar cell material and device characterization," in *Proc. 25th IEEE Photovolt. Spec. Conf.*, Washington, DC, USA, 1996, pp. 457–460.
- [59] H. Nagel, C. Berge, and A. G. Aberle, "Generalized analysis of quasi-steady-state and quasi-transient measurements of carrier lifetimes in semiconductors," *J. Appl. Phys.*, vol. 86, pp. 6218–6221, 1999.
- [60] W. A. Lanford and M. J. Rand, "The hydrogen content of plasma-deposited silicon nitride," *J. Appl. Phys.*, vol. 49, pp. 2473–2477, 1978.
- [61] S. Joos *et al.*, "Fundamental studies of hydrogen at the silicon / silicon nitride interface," *Energy Procedia*, vol. 55, pp. 786–790, 2014.
- [62] N. M. Johnson, F. A. Ponce, R. A. Street, and R. J. Nemanich, "Defects in single-crystal silicon induced by hydrogenation," *Phys. Rev. B*, vol. 35, pp. 4166–4169, 1987.
- [63] S. B. Zhang and W. B. Jackson, "Formation of extended hydrogen complexes in silicon," *Phys. Rev. B*, vol. 43, pp. 12142–12145, 1991.



**Axel Herguth** received the Diploma degree in physics from the University of Konstanz, Konstanz, Germany, in 2006.

Since 2007, he has been the Head of the characterization group with the Photovoltaics Division, University of Konstanz. His research interests include the kinetics of defects in silicon in general, especially the kinetic of the boron–oxygen-related defect, as well as characterization techniques for silicon wafers and solar cells.

Mr. Herguth was a recipient of the Junior Einstein Award from Solarworld in 2006 for his work on the avoidance of the boron–oxygen-related degradation.



**Christian Derricks** received the master's degree in physics from the University Duisburg-Essen, Duisburg, Germany, in 2013. Since 2016, he has been working toward the Ph.D. degree in degradation and regeneration effects in mono- and multicrystalline silicon solar cells at the Photovoltaic Division, University of Konstanz, Konstanz, Germany.



**David Sperber** received the Diploma degree in physics from the Karlsruhe Institute of Technology, Karlsruhe, Germany, in 2013. Since 2014, he has been working toward the Ph.D. degree at the Photovoltaics Division, University of Konstanz, Konstanz, Germany.

His research interests include the lifetime stability of crystalline silicon and related surface passivation. He is especially interested in light-induced changes of lifetime and changes caused by high-temperature steps.